Journal of Groundwater Science and Engineering
ISSN 2305-7068
Indexed by ESCI CABI CSA
Scopus GeoRef AJ CNKI

Multi-scale characterization of karst media, negative-pressure suffusion mechanism and collapse risk assessment for urban metro engineering: A case study of Guiyang metro line 3, China

Lei Zhang, Xiang-quan Li, Jian-fei Ma, Zhen-yuan Zhang, Chang-chang Fu, Chun-chao Zhang, Ce Zhang

Citation:
Zhang L, Li XQ, Ma JF, Zhang Z-Y, Fu C-C, Zhang C-C, Zhang C. 2026. Multi-scale characterization of karst media, negative-pressure suffusion mechanism and collapse risk assessment for urban metro engineering: A case study of Guiyang metro line 3, China. Journal of Groundwater Science and Engineering, 14(3): 307-322.

View online: https://doi.org/10.26599/JGSE.2026.9280084

Articles you may be interested in

Health risk assessment of heavy metal pollution in groundwater of a karst basin, SW China
Journal of Groundwater Science and Engineering. 2024, 12(1): 49-61 https://doi.org/10.26599/JGSE.2024.9280005

Health risk assessment of Fluoride and Cadmium enrichment in rural drinking groundwater in Shanxi Province, China
Journal of Groundwater Science and Engineering. 2026, 14(1): 1-14 https://doi.org/10.26599/JGSE.2026.9280067

Ecological vulnerability assessment and driving force analysis of small watersheds in Hilly Regions using sensitivity-resilience-pressure modeling
Journal of Groundwater Science and Engineering. 2025, 13(3): 209-224 https://doi.org/10.26599/JGSE.2025.9280050

Causes and health risk assessment of fluorine in the Red bed groundwater and adjacent geothermal water of the Guang'an Area, Southwest China
Journal of Groundwater Science and Engineering. 2025, 13(2): 116-132 https://doi.org/10.26599/JGSE.2025.9280043

Critical issues in the characteristics and assessment of China's water resources
Journal of Groundwater Science and Engineering. 2024, 12(4): 463-474 https://doi.org/10.26599/JGSE.2024.9280033

Characterization of rock thermophysical properties and factors affecting thermal conductivity–A case study of Datong Basin, China
Journal of Groundwater Science and Engineering. 2024, 12(1): 4-15 https://doi.org/10.26599/JGSE.2024.9280002

Journal homepage: http://gwse.iheg.org.cn

Research Article

Multi-scale characterization of karst media, negative-pressure suffusion mechanism and collapse risk assessment for urban metro engineering: A case study of Guiyang metro line 3, China

Lei Zhang[1,2], Xiang-quan Li[1,2*], Jian-fei Ma[1,2], Zhen-yuan Zhang[3], Chang-chang Fu[1,2], Chun-chao Zhang[1,2], Ce Zhang[4]

[1] *Institute of Hydrogeology and Environmental Geology*, *Chinese Academy of Geological Sciences*, *Shijiazhuang* 050061, *China*.
[2] *Key Laboratory of Groundwater Sciences and Engineering*, *Ministry of Natural Resources*, *Shijiazhuang* 050061, *China*.
[3] *School of Engineering and Technology*, *China University of Geosciences(Beijing)*, *Beijing* 100083, *China*.
[4] *Guiyang Rail Transit Line 3 Construction and Operation Co., Ltd.*, *Guiyang* 550025, *China*.

Abstract: Multi-scale characterization of karst media is a fundamental prerequisite for accurate stability evaluation and collapse risk assessment in karst terrains, especially for the safety control of urban metro engineering. Taking the Huaxi South Parking Lot of Guiyang metro line 3 as a case study, this paper proposes an integrated framework for karst collapse risk assessment by coupling multi-scale geological characterization, hydrodynamic-mechanical coupling simulation, and spatial multi-factor analysis. A comprehensive dataset, including 339 borehole records, core CT scanning results, long-term hydrogeological monitoring data, and laboratory test results, was collected to conduct multi-scale characterization of karst media across macro, meso and micro scales, reveal the vertical zonation of karst structures, clarify the hydrodynamic triggering mechanism of karst collapse, determine the critical instability threshold, and reproduce the entire evolution process of collapse. The results show that negative-pressure suffusion induced by rapid groundwater level decline, with a critical pressure difference of ≤ −190 kPa, is the dominant trigger of karst collapse in the study area. The lowest stratum stability and highest collapse risk occur in the strata with an overburden thickness of 2–5 m and a karst cavity diameter of ≥ 3 m. The high-risk zones account for 2.3% of the total study area, and are mainly distributed in the southern part, while the overall site remains stable under normal hydrodynamic conditions. This study can provide theoretical support and technical reference for karst collapse risk prevention and control in urban metro engineering.

Keywords: Karst collapse; Media characterization; Negative-pressure suffusion; Critical collapse threshold; Risk assessment

Received: 08 Nov 2025/ Accepted: 15 Mar 2026/ Published: 30 Jul 2026

Introduction

Negative environmental impacts resulting from altered groundwater conditions are widespread in China (Zhang et al., 2015; Ling et al., 2024). Urbanization has subtly transformed groundwater characteristics, making regions highly susceptible to catastrophic events. In karst cities, rapid urban development and growing demands for public infrastructure construction pose significant challenges.

As urbanization in China accelerates, the demand for public infrastructure, particularly metro networks, has increased to alleviate traffic congestion and enhance mobility (Cui et al., 2015; Wang et al., 2017; Li et al., 2020). However, metro construction and operation in karst regions often lead to engineering hazards such as ground collapse, water inrush, and shield machine failures,

*Corresponding author: Xiang-quan Li, *E-mail address*: 1711039960@qq.com

DOI: 10.26599/JGSE.2026.9280084

Zhang L, Li XQ, Ma JF, et al. 2026. Multi-scale characterization of karst media, negative-pressure suffusion mechanism and collapse risk assessment for urban metro engineering: A case study of Guiyang metro line 3, China. Journal of Groundwater Science and Engineering, 14(3): 307-322.

2305-7068/© 2026 Journal of Groundwater Science and Engineering Editorial Office This is an open access article under the CC BY-NC-ND license (http://creativecommons.org/licenses/by-nc-nd/4.0)

with collapses posing significant risks. These incidents can cause ground settlement, impacting surface structures and threatening public safety and property. Notable cases include the Wuhan Metro (Shen et al., 2014), Jinan Metro (Cui et al., 2015; Kang et al., 2021), and Guiyang Metro (Feng, 2020; Zhang et al., 2018; Liu et al., 2022). Therefore, a thorough assessment of collapse risks along metro alignments in karst cities is essential for ensuring engineering safety.

Guiyang, the sole city in Guizhou Province with a functioning metro system, operates four lines through extensively developed karst formations (Zhang et al., 2018; Zhang et al., 2022; Wang et al., 2018). Excavations in these geologically intricate areas, exacerbated by extreme hydrologic events such as rainstorms and human-induced pumping, greatly increase the risk of karst collapses. This risk is intrinsically linked to multi-scale geological structures and dynamic hydrogeological processes. Existing research primarily addresses either single-scale karst features, such as macroscopic cavity detection, or static risk assessments (Zhang et al., 2025; Zhang et al., 2022; Yang et al., 2024). A significant knowledge gap remains in understanding the interactions between microscopic pore networks and macroscopic hydrodynamic processes, which impedes accurate identification of the dynamic failure mechanisms driving collapse events.

Traditional karst collapse risk assessment predominantly employs geophysical methods to detect large-scale karst structures but fails to adequately capture submillimeter-scale heterogeneity in micropores and fractures (Ba et al., 2020). Simultaneously, static hydrological models are unable to simulate transient pressure dynamics during extreme events, such as rapid water-level declines, impeding the quantitative determination of collapse thresholds. Existing risk zoning models often rely on single-factor overlays without integrating multi-scale data or validating hydrodynamic mechanisms (Zhang et al., 2022, He et al., 2014; He et al., 2013; Yang et al., 2025; Zhou et al., 2022), thereby reducing prediction accuracy. This study introduces an integrated "Multi-scale Characterization Hydrodynamic Modeling-Risk Zonation" framework, using Guiyang Huaxi South Parking Lot (HxS-PL) as a case study, with three main objectives: (1) Multi-scale karst characterization: Quantify vertical zonation of karst features across macroscopic (>1 m), mesoscopic (1 mm–1 m), and microscopic (<1 mm) scales using drilling, CT scanning, and 3D modeling to reveal the spatial evolution of pores, fractures, and cavities. (2) Dynamic hydrodynamic analysis: Simulate pressure-field variations under normal and extreme hydrologic conditions using COMSOL Multiphysics and PFC2D to identify critical thresholds. (3) Risk assessment innovation: Develop a coupled-factor collapse risk zoning model integrating the Analytic Hierarchy Process (AHP) and GIS spatial analysis, providing a scientific basis for mitigating urban underground engineering risks. This research surpasses conventional single-scale methods through multiphysics coupling and dynamic threshold analysis, enhancing the mechanistic understanding of karst collapse processes. The findings are directly applicable to the design, construction, and maintenance of underground infrastructure in karst regions, offering significant theoretical and practical value.

1 Study area

The study area is located at the HxS-PL of Guiyang Metro Line 3 in Huaxi District, Guizhou Province (Fig. 1a). The long-term average annual precipitation is 1,136.96 mm, with a maximum of 1,760.8 mm recorded in 1954. Precipitation across the region is unevenly distributed throughout the year, with the majority falling between April and August, accounting for approximately 60% of the annual total (Fig. 1b). Geographically, this region features a north-to-south gradient, with higher elevations in the north and lower in the south. The rail maintenance depot and integrated development tower areas lie within a karst denudation landform marked by low-hill depressions. The core zone is near the northern uplifted axis of the Guiyang Syncline, adjacent to the Qianling Mountain residual karst hills in the northern part of the Guiyang karst basin.

The study area comprises Quaternary anthropogenic fill (Q_4^{ml}), residual and slope wash deposits (Q_4^{el+dl}), and Triassic Songzikan Formation (T_2sz) strata. The Quaternary overburden, varying in thickness from 0.2 m to 20.8 m, includes fill soil, red clay, and gravelly soil, with basal elevations ranging from 1,067.07 m to 1,086.35 m. The bedrock is composed of dolomite, ranging from strongly to moderately weathered, displaying a massive structure with well-developed joint fissures. Regionally, the Huaxi Fault and Zhongcaosi Syncline are the main geological structures, with no major structures crossing the site. The area features a dual aquifer system—comprising pore water and karst water—that drains southward to the Qingyan Spring discharge point.

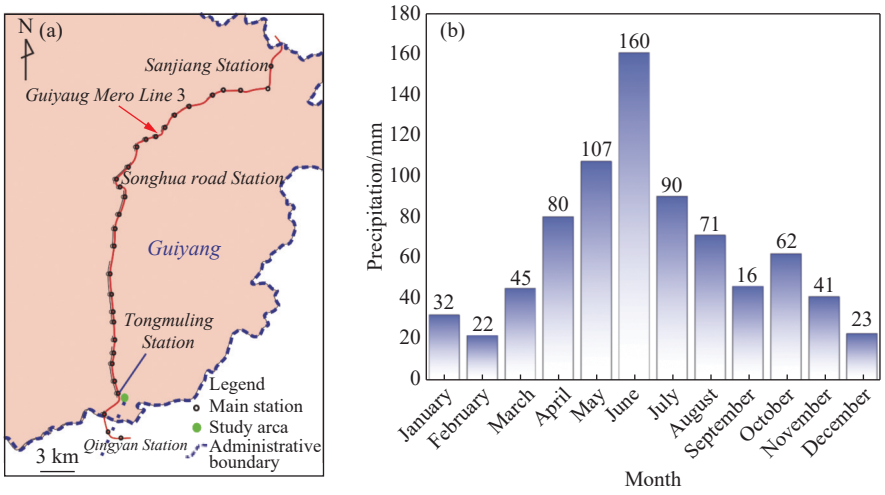


Fig. 1 Overview of the study area

Notes: (a) location of the study area; (b) monthly average precipitation patterns with heavy rainfall occurring primarily from April to August

2 Materials and methods

2.1 Data collection

(1) Geophysical exploration and drilling

The analysis of 339 boreholes at the site identified structural features of cavities and their geological context, forming a foundational database for assessing collapse risk. Key parameters include cavity roof and floor depths, overburden thickness, cover thickness above the cavity roof, and the vertical distance between the cavity floor and the primary karst water table-essential for evaluating karst collapse susceptibility. Concurrently, geophysical surveys pinpointed instrumented boreholes intersecting cavities to explore subsurface karst distribution. Drilling to a depth of 86 m yielded core recovery logs, RQD values, and karstification ratios, which are crucial for understanding stratigraphic architecture and dissolution heterogeneity.

(2) Hydrologic monitoring

A multiparameter borehole monitoring system was deployed to collect real-time field and subsurface data, capturing the dynamic behavior of the primary karst aquifer. Continuous measurements of barometric pressure, precipitation, turbidity, and water-table depth were recorded from April 29 to December 31, 2024, over a 238-day period, as illustrated in Fig. 2.

2.2 Analytical method

(1) Multi-scale characterization of core structure

Utilizing techniques such as core measurement, image analysis, fractal dimension calculation, and CT scanning, this study gathers comprehensive data on karst pores and cavities. This facilitates

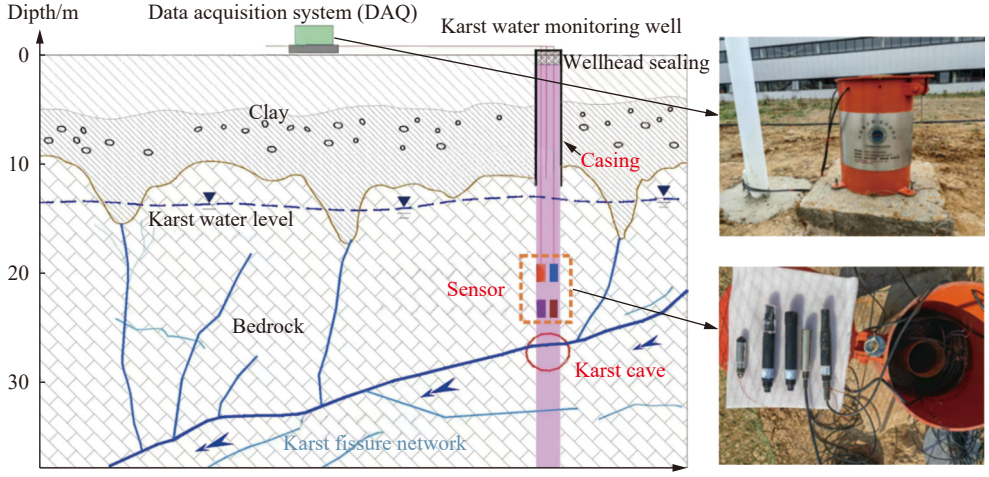


Fig. 2 Schematic diagram of the monitoring device principle

multi-scale characterization of karst structures, spanning macro to micro levels, and provides a scientific foundation for understanding karst collapse mechanisms and predicting related disasters. At the macroscopic level, borehole distribution is statistically analyzed to discern overburden and bedrock development patterns, revealing vertical stratigraphic layers and defining karst development zones and their depth ranges. At the mesoscopic level, "Cloudy Earth" software constructs 3D visual models of intact core samples, using core photographs comprising at least 16 images per side and separately photographed end sections. ImageJ processes these images to analyze microstructural features. At the microscopic scale, CT scanning quantifies parameters like average porosity, pore volume, and average throat radius at varying core depths, characterizing core dissolution pores, fissures, and fracture media.

(2) Numerical calculation

This study evaluates the karst collapse risk at HxS-PL in Guiyang City by integrating theoretical calculations with numerical simulations. Using borehole data and geological cross-section characteristics, we developed collapse mechanics and numerical simulation models. Considering the site's karst geological features and dynamic groundwater monitoring data, we employed COMSOL Multiphysics and PFC2D to create a multiphysics coupling model. This model assesses hydrostatic pressure variations under normal and extreme conditions. COMSOL Multiphysics specifically simulated hydrostatic pressure changes in the overburden layer based on monitored water levels, with parameters detailed in Table 1. The governing equations adhere to Darcy's Law (Equation (1)).

$$q = -K\nabla h \tag{1}$$

Where: q is the seepage velocity, K denotes the permeability coefficient, and ∇h represents the hydraulic gradient.

A numerical simulation model was developed based on the stratigraphic characteristics of the study area. A one-dimensional coupled analysis was conducted to evaluate the risk of karst collapse under both actual and extreme water level fluctuations, using data from monitoring boreholes. The simplified geological model, depicted in Fig. 3, consists of four layers: Layer I includes the overburden with plain fill, laterite, and gravel; Layer II is a strongly weathered bedrock fracture zone; a karst cave (water level: −17 m) lies between Layers II and III; Layers III and IV contain a second karst cave (water level: −35 m). Hydraulic pressure monitoring points were positioned at coordinates A (40 m, −2 m), B (40 m, −5 m), and C (40 m, −9 m) within the soil layers to simulate pressure changes during groundwater level variations.

As actual calculations require continuous media, equivalent treatments must be applied to fractures and karst cavities. Fractures are assumed to be filled with water and their density is set to the same value as water. Karst cavities are primarily filled with air and surrounded mainly by bedrock; thus, their parameters are set to a density greater than that of water, but similar to that of clay, which is equivalent to that of a porous medium.

The PFC2D model utilized averaged stratigraphic thicknesses from the site, dividing it into three layers: Plain fill, laterite, and gravel, with thickness ratios of 3:6:1 and particle sizes between 0.03–0.11 m. A scaled numerical model, 1 m long and 0.2 m high, was created, comprising 5,560 particles. The lateral boundaries were horizontally fixed, the top surface was free, and three wall segments of varying lengths were removed at the base to simulate fracture channels in the bedrock, with widths of 0.04 m, 0.06 m, and 0.04 m. Fixed walls ensured stability in the bedrock zone. Hydrostatic pressure under normal water levels, simulated using COMSOL Multiphysics, was applied in the PFC2D model to analyze deformation and failure of the overburden under both standard and extreme water levels. Nine monitoring points were placed, mainly in bedrock fracture zones and stratigraphic interfaces, with displacement tracked at the

Table 1 Computation parameters for the COMSOL multiphysics model

Rock and Soil Properties	Density (kg/m^3)	Porosity	Permeability (m^2)	Dynamic viscosity (Pa·s)
Plain fill	1,730	0.45	5×10^{-6}	0.001
Red clay	1,730	0.5	1×10^{-9}	
Gravel soil	2,000	0.6	1×10^{-4}	
Bedrock	2,500	0.25	1×10^{-12}	
Fissure	1,000	0.8	1×10^{-3}	
Karst cave	1,500	0.3	1×10^{2}	

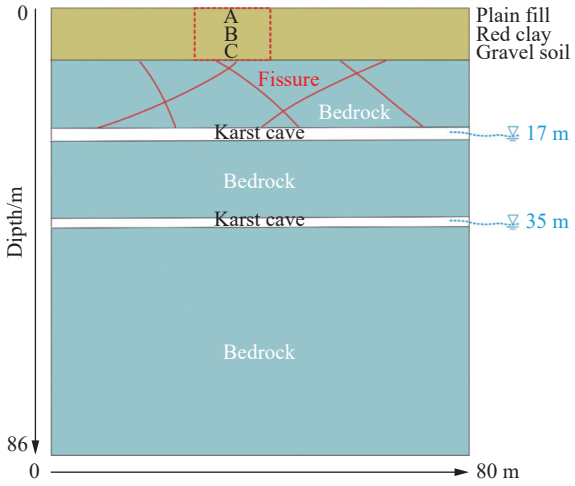


Fig. 3 COMSOL Multiphysics numerical computation model

center of each region. Computational parameters are detailed in Table 2, and the model is depicted in Fig. 4. The mesoscopic parameters in Table 2 were calibrated through numerical "virtual experiments" to match the macroscopic mechanical behavior of the soils listed in Table 1.

(3) Analysis of collapse critical threshold

Utilizing COMSOL Multiphysics simulations, the threshold for pressure differential variations due to water level changes was established. Hydrodynamic analysis identified suction-induced collapse as the potential mechanism. Based on prior research and borehole data on karst cave features (Wang et al., 2011; Yao et al., 2018), we calculated criteria for direct-contact karst collapse in the overburden. The theoretical model assumes: (1) an elliptical collapse pit approximated as a circular pit with diameter D; (2) a karst cave with vertical sidewalls spanning D'; (3) overburden soil failure follows the Mohr-Coulomb criterion; (4) overburden thickness above the cave is h, with cavity height h_1 and overburden thickness h_2 above the cavity roof; (5) the angle between the cave sidewall sliding surface and vertical is β; (6) the horizontal distance from the cave to the pit edge is a. The collapse process is modeled in three stages: soil cavity formation, barrel-shaped surface collapse, and funnel-shaped collapse. The model is depicted in Fig. 5.

Based on borehole data from the site, the thickness range of the overburden was determined. The critical thickness for soil arching development is derived as follows (Wang et al., 2011):

$$h_2 = h - 0.828\frac{D - 2h\cdot\tan\left(45^\circ - \frac{\varphi}{2}\right)}{2f_k} \tag{2}$$

Where: f_k is the soil cohesion coefficient, and φ denotes the internal friction angle.

Substituting the pressure differential range obtained from numerical simulations into the safety factor calculation formula yields (Wang et al., 2011):

$$k = \frac{\frac{4}{D'}\left[\frac{k_0\cdot\gamma\cdot h_2^{\,2}}{2}\tan\varphi + c\cdot h_2\right]}{\gamma\cdot h_2 + \triangle p} \tag{3}$$

Table 2 Mesoscopic Parameters for Numerical Simulation

Material	Density (kg/m^3)	Porosity	r_{max}	r_{min}	Stiffness ratio	Friction coefficient	Normal bond strength/kPa	Shear bond strength/kPa
Plain fill	1,743	0.32	0.0042	0.0032	2	0.5	20	10
Red clay	1,600	0.4	0.0030	0.0023	1.5	0.8	75	50
Gravel soil	1,800	0.24	0.0055	0.0021	2	0.8	200	100

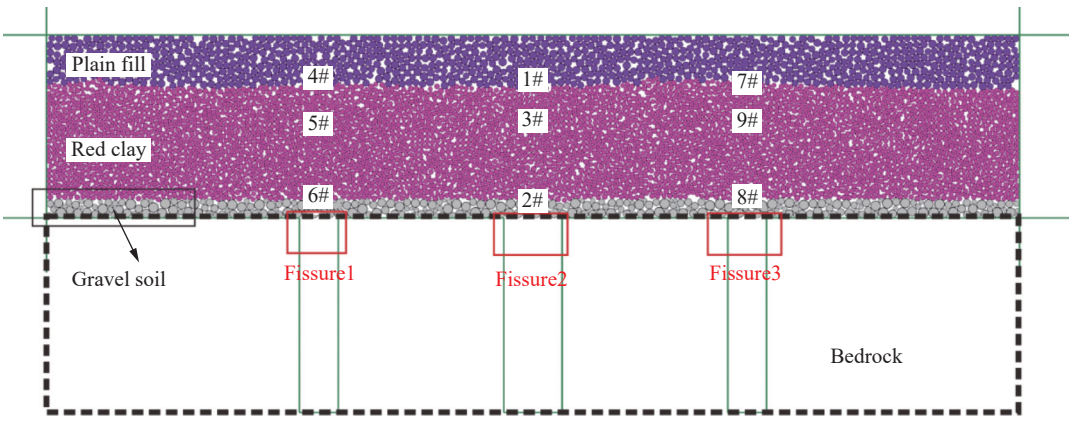


Fig. 4 PFC2D numerical computation model

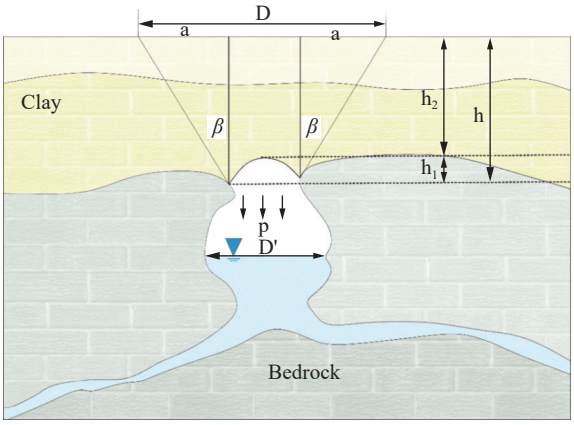


Fig. 5 Computational schematic for the suction-induced collapse mechanism

Where: $\triangle p$ denotes the pressure differential, γ represents the unit weight of the soil, c is the cohesion, and k_0 is the coefficient of earth pressure at rest. We analyzed the variation in the soil stability safety factor across different overburden thicknesses to determine the collapse threshold for the study area. Stability is indicated by $k > 1$, a critical state by $k = 1$, and instability by $k < 1$, where k is the safety factor Fs.

(4) Risk assessment and verification

The Analytic Hierarchy Process (AHP) was used to develop a risk assessment index system for karst collapse, featuring three primary indicators: Karst development intensity, overburden characteristics, and hydrodynamic conditions, along with eight secondary indicators (Table 3). Utilizing calculated threshold values, spatial overlay analysis was performed to obtain the final risk assessment outcomes.

3 Results and discussion

This study precisely characterized the karst structures and hydrogeological conditions of the site using integrated methods such as geological surveys, CT scans of borehole cores, hydrodynamic monitoring, and multiphysics coupling simulations. It evaluated critical collapse thresholds and developed a risk assessment index system. Based on spatial analysis and threshold evaluations, the collapse risk was comprehensively determined. The main findings are summarized as follows.

3.1 Multi-scale karst structural characteristics

Macro-scale

Karst development patterns at the site were assessed using borehole core RQD, karst ratio characteristics, and core structure. Analysis of overburden thickness from 110 borehole-exposed karst caves shows a maximum of 20.9 m, a minimum of 1.8 m, fluctuations around 8 m, and an average of about 9 m. Identical overburden thicknesses at some locations suggest multi-level caves within single boreholes. Most caves are under 3 m in height, indicating a "small but numerous" pattern. Cave elevations are mainly between 106–107 m, with burial depths of 10–20 m.

The bedrock cores have an overall RQD (Rock Quality Designation) of 36% (Fig. 6a), with a total core length exceeding 10 cm measuring 30.96 m. RQD per meter shows a trend of "higher in upper sections, lower in deeper sections". Below 33 m, most 1-meter RQD values surpass the overall average. The highest RQD (>90%) is at 23–25 m depth, with maximum single-core segments over 0.4 m. Below 56 m, core fragmentation increases markedly, with some intervals resembling "gravel-like fragments". From 70 m to the borehole bottom, no cores exceed 10 cm, resulting in an RQD of 0.

Fig. 6b depicts the correlation between linear and areal karst ratios at various depths. Linear karst ratios span from 0% to 14%, with an average of 1.49%, peaking at 14% at a depth of 43–44 m, indicating maximum linear karst density. Areal

Table 3 Karst collapse risk assessment index system

Target Layer	Tier-1 Indicators	Tier-2 Indicators
Karst collapse risk assessment (K)	Karst development intensity (A1)	Borehole karst encounter rate (B1)
		Karst cave development height (B2)
		Karst cave development depth (B3)
	Overburden characteristics (A2)	Overburden structure (B4)
		Overburden thickness (B5)
		Distance to karst cave roof (B6)
	Hydrodynamic conditions (A3)	Groundwater level distance to overburden base (B7)
		Groundwater level to phreatic surface distance (B8)

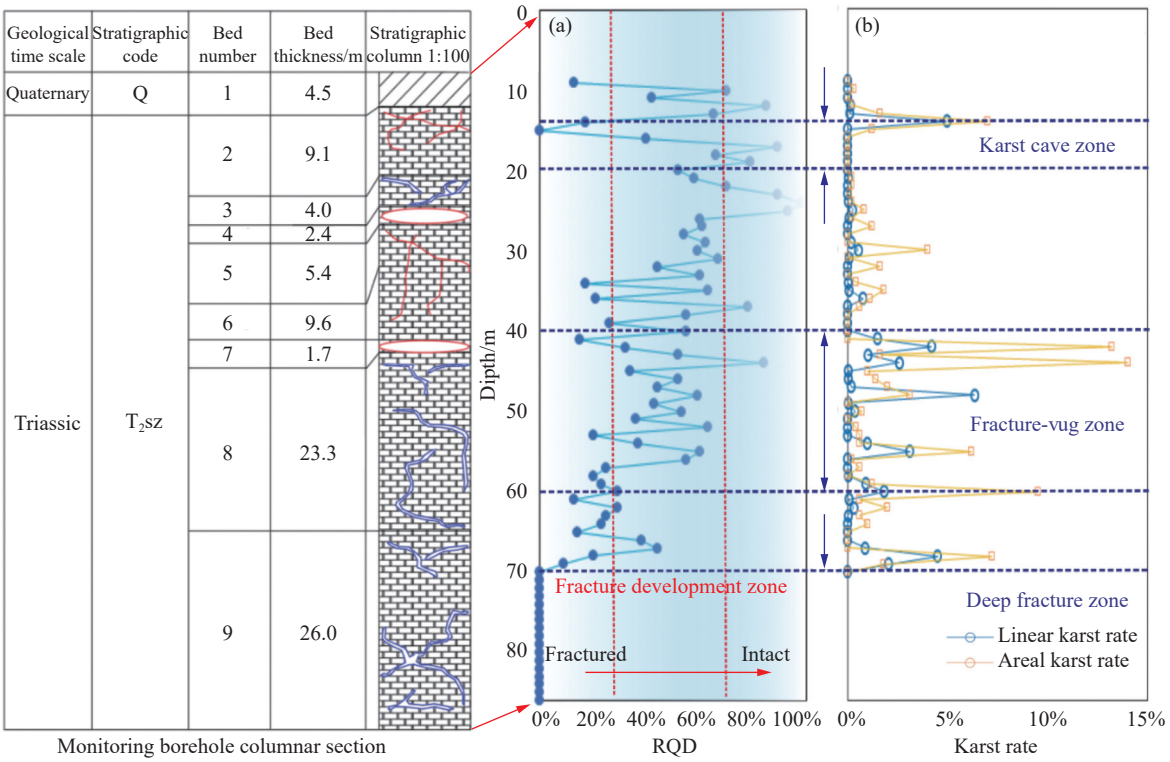


Fig. 6 Comprehensive analysis of core data from the monitoring borehole ((a) Core RQD; (b) Core karst ratios)

karst ratios show a similar trend, with a maximum of 6.34%, a minimum of 0%, and an average of 0.61%. The peak depths differ due to positional discrepancies during data collection, yet both metrics consistently reflect karst patterns.

Integrating these findings with geological surveys, macro-scale karst development patterns were identified. Core data from the monitoring borehole reveal four stratigraphic intervals: (1) Overburden (0–4.5 m); (2) Karst cave development (15–20 m); (3) Fracture-dissolution fissure (40–60 m); and (4) Deep fracture development (>70 m). The lower boundary of karst development in the study area is established at a depth of 70 m.

Meso-scale

Using high-precision measurements, 3D modeling, and image analysis, karst density and fractal dimension metrics were developed to characterize meso-scale (10^{-3}–10^{-1} m) karst structures (Fig. 7). The findings indicate significant heterogeneity in dissolution pore development and morphology at various depths. Maximum pore cross-sectional dimensions are observed at depths of 15–17 m and 47–48 m, with major axes measuring 2.9–3.1 cm and aspect ratios near 1. Higher fractal dimensions were detected at depths of 9–12 m, 16–18 m, 20–23 m, 35–40 m, and 47–49 m, suggesting intensified dissolution. Notably, strong fluctuations in fractal dimension curves with elevated averages of 1.859 and 1.857 characterize the 9–34 m and 43–64 m intervals, while other sections show stable curves with a mean dimension of 1.83, confirming increased dissolution intensity in these zones.

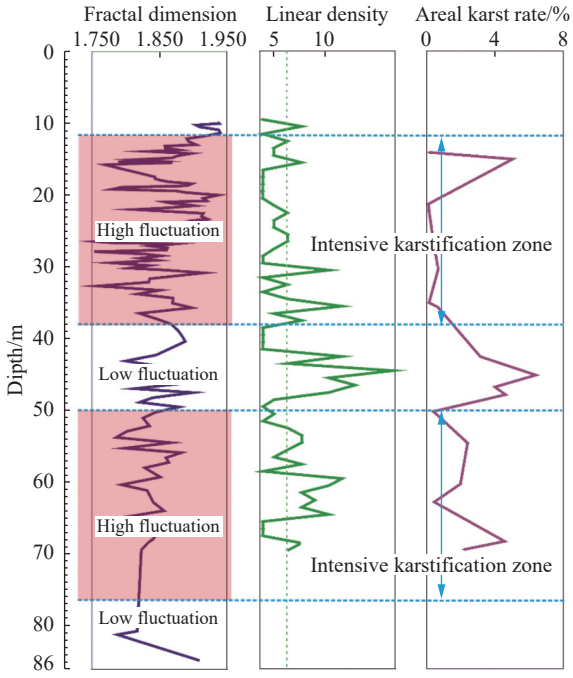


Fig. 7 Meso-scale metrics of the monitoring borehole

Micro-scale

Core CT scanning was utilized to obtain micro-scale parameters (10^{-6}–10^{-3} m) such as dissolution

pore diameter, shape factor, throat length, pore-throat diameter ratio, and tortuosity, which characterize karst structures and differentiate dissolution pores from fracture media. At this scale, dissolution pores have average radii of 56.51–110.37 μm and median radii of 156.41–2,634 μm. The largest average (91.34–110.37 μm) and median (820–2,634 μm) pore radii are found at depths of 46–48 m. Shape factors consistently range from 0.029 to 0.031, indicating minimal morphological variation among micro-scale voids. Tortuosity values above 2 at depths of 26–27 m, 42–43 m, and 54–55 m indicate complex pore structures. At 46–48 m, reduced tortuosity values (1.84–1.89) result from larger pores connecting smaller throats. Below 60 m, increased tortuosity and dimensions correlate with fracture development in deep zones. Beyond 69 m depth, throat radii reach 1,752.48 μm, significantly larger than those at other depths (120.66–198.54 μm), with fewer dissolution pores, indicating dominant fracture media characteristics.

Analysis of representative cores reveals distinct microstructural features within the monitoring borehole, as shown in Fig. 8. At the microscale (10^{-6}–10^{-3} m), voids above 69 m depth are primarily dissolution pores with average radii between 10^{-5} m and 10^{-4} m. The most significant dissolution occurs at 46–48 m depth, where pores have average radii of 110.37 μm, and throat lengths range from 120.66 μm to 198.54 μm, indicating well-developed fracture media characteristics. Below 69 m depth, fractures dominate the void systems, with significantly elongated throat lengths of 1,752 μm and reduced dissolution activity.

3.2 Hydrodynamic triggering mechanism

Dynamic characteristics of groundwater

Real-time borehole data reveal key hydrogeological features of the study area: Groundwater levels range from 7.24 m to 18.54 m, averaging 11.4 m. Annual fluctuations typically span 3–5 m. The wet season occurs in June–July, and the dry season in November-December. Water levels show rapid minor oscillations during wet periods and larger, sustained declines in dry periods. Changes in

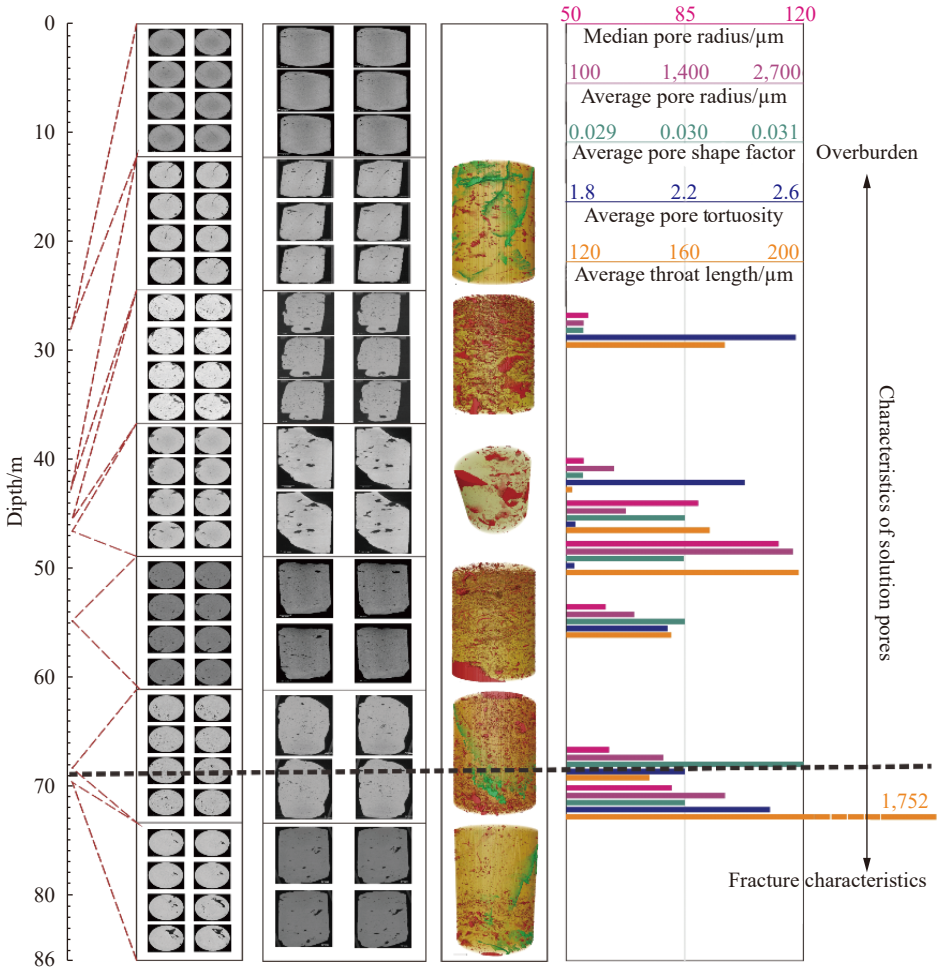


Fig. 8 Microstructural characteristics of cores from the monitoring borehole

groundwater depth correlate with rainfall intensity, as shown in Fig. 9. In 2024, the maximum intraday water level rise was 1.5 m, with a 5-d cumulative rise of 3.5 m. Regarding turbidity, post-borehole completion saw a rapid peak at 534.1 NTU under certain rainfall conditions, stabilizing thereafter. Once stabilized, turbidity did not correlate with rainfall intensity, indicating stable groundwater quality with transient turbidity spikes only during initial aquifer penetration.

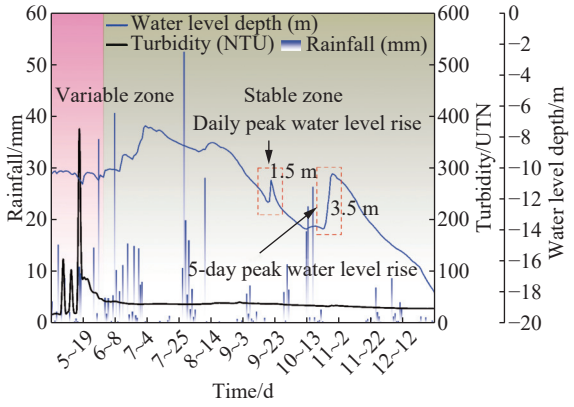


Fig. 9 The curve of turbidity varying with rainfall

Characteristics of pressure difference variation

The fitted function representing actual water level fluctuations was integrated into COMSOL Multiphysics to simulate seepage field characteristics under observed hydrodynamic conditions. As depicted in Fig. 10, the trend of the fitted function closely matches the measured water level fluctuations, confirming its suitability for computational modeling. Analysis of the soil depth profile (Fig. 11) indicates that superficial soil layers remain unaffected by deeper seepage fields under these water level changes, highlighting the low permeability of laterite. The gravel layer and basal

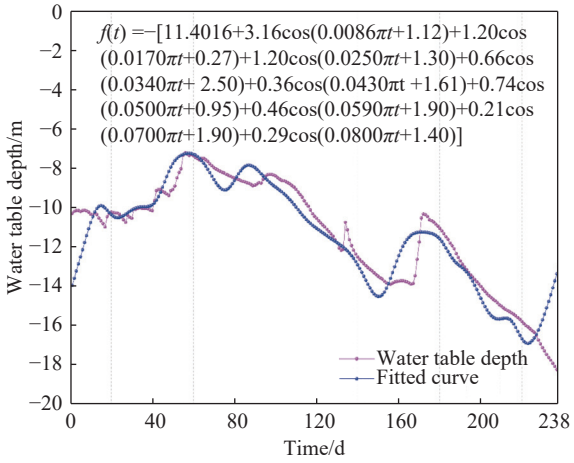


Fig. 10 Measured water levels and fitted function curves

laterite are critical for collapse initiation. Prolonged groundwater erosion at the soil-rock interface weakens structural integrity, increasing collapse risk, especially where karst caves are minimally separated from overlying soil layers.

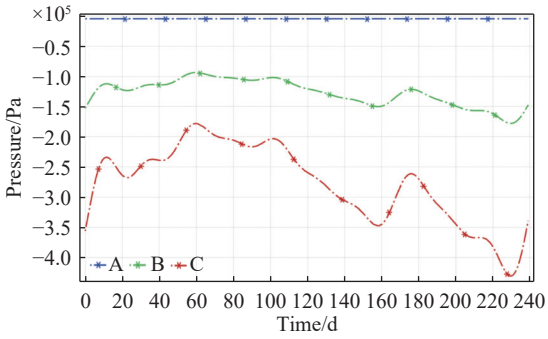


Fig. 11 Hydrostatic pressure monitoring curves

To assess pressure variations across soil layers under normal water level fluctuations, the hydrostatic pressure during this period served as the baseline. Simulations revealed pressure differentials across soil strata, providing essential data for subsequent particle flow numerical modeling of karst collapse. Fig. 12 presents these findings. The gravel layer showed a maximum negative pressure differential of −190 kPa and a maximum positive differential of 62.6 kPa. This suggests that sustained water level decline in the area can lead to extreme negative pressure differentials of −190 kPa, and such values, if reached instantaneously due to engineering disturbances, may trigger suction-induced collapse.

Analysis of the collapse process caused by negative pressure erosion

The collapse evolution process was simulated using PFC2D numerical modeling software, informed by the fitted water level monitoring curve, with results shown in Fig. 13. Initially, tensile cracks primarily emerged at soil layer inter-

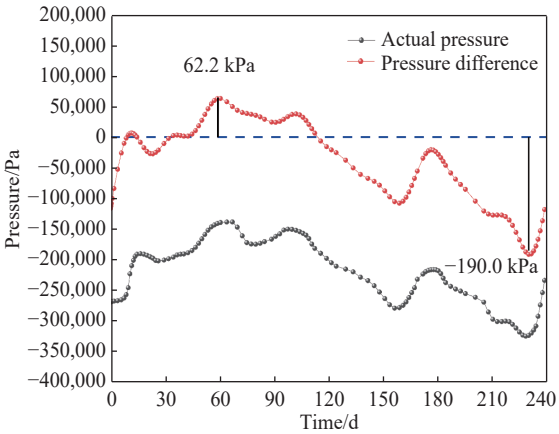


Fig. 12 Pressure differential variation trend

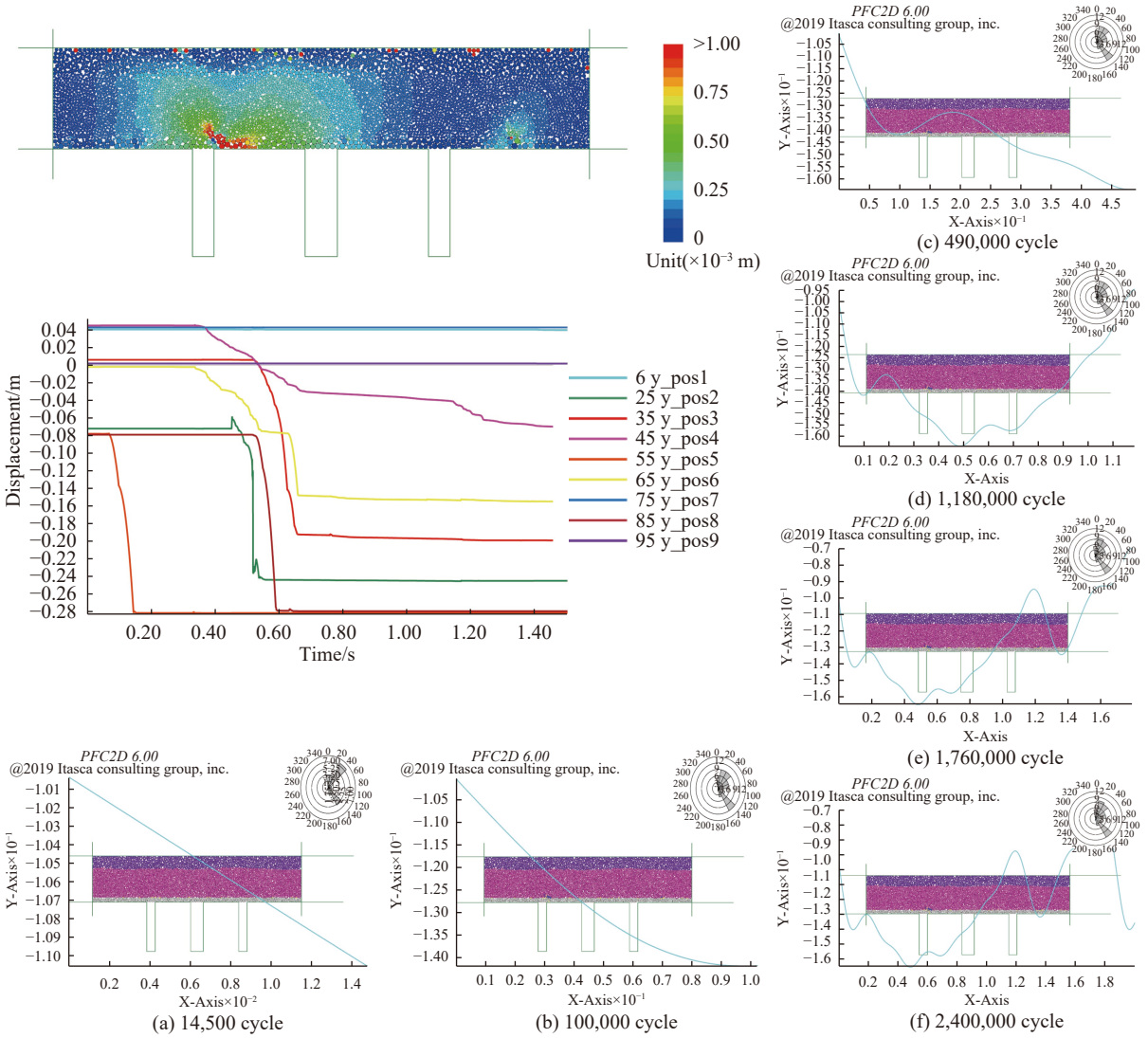


Fig. 13 Displacement contour plots and evolution characteristics under normal monitored water level fluctuations

faces, coinciding with the first water level fluctuation. Crack orientations were mainly between 0° and 150°, with a higher density from 130° to 150°, indicating dominant tensile stress perpendicular to these directions. A secondary concentration of cracks at 10°–45° may be attributed to lateral particle sliding constrained by underlying bedrock. Importantly, no significant deformation occurred under natural water levels, where interfacial cracking was the primary factor affecting stratum stability. During normal water level fluctuations, the strata remained globally stable, with localized cracks developing along layer interfaces.

Assuming a rapid decline of the water table at 1.5 m/d, a scaling function (Equation (4)) was employed to simulate collapse development characteristics under extreme water drawdown conditions.

$$h = -0.1 - 1.5 \cdot t \tag{4}$$

Fig. 14a illustrates the initial state of the calculation model. As the decline begins (Fig. 14b), numerous fractures emerge at the formation interface, creating an arch-like pattern along the "bedrock" fracture boundary. After 0.28 seconds, the gravel layer above the left fracture collapses first (Fig. 14c), leading to the formation and upward expansion of arch holes. Soil particles on both sides of this expansion become disturbed, enlarging the deformation area (Fig. 14d). By 0.68 seconds, this deformation reaches the surface, causing partial collapse (Fig. 14e). The collapse area resembles a leakage cylinder, obstructing the fractured pipe below (Fig. 14f). Concurrently, a similar failure occurs in the middle fracture, transforming it into a soil cavity that collapses from bottom to top, forming a vertical free surface (Fig. 14g). This cavity then expands laterally, creating a larger void (Fig. 14h), which significantly impacts the stability of the entire stratum, ultimately leading to collapse.

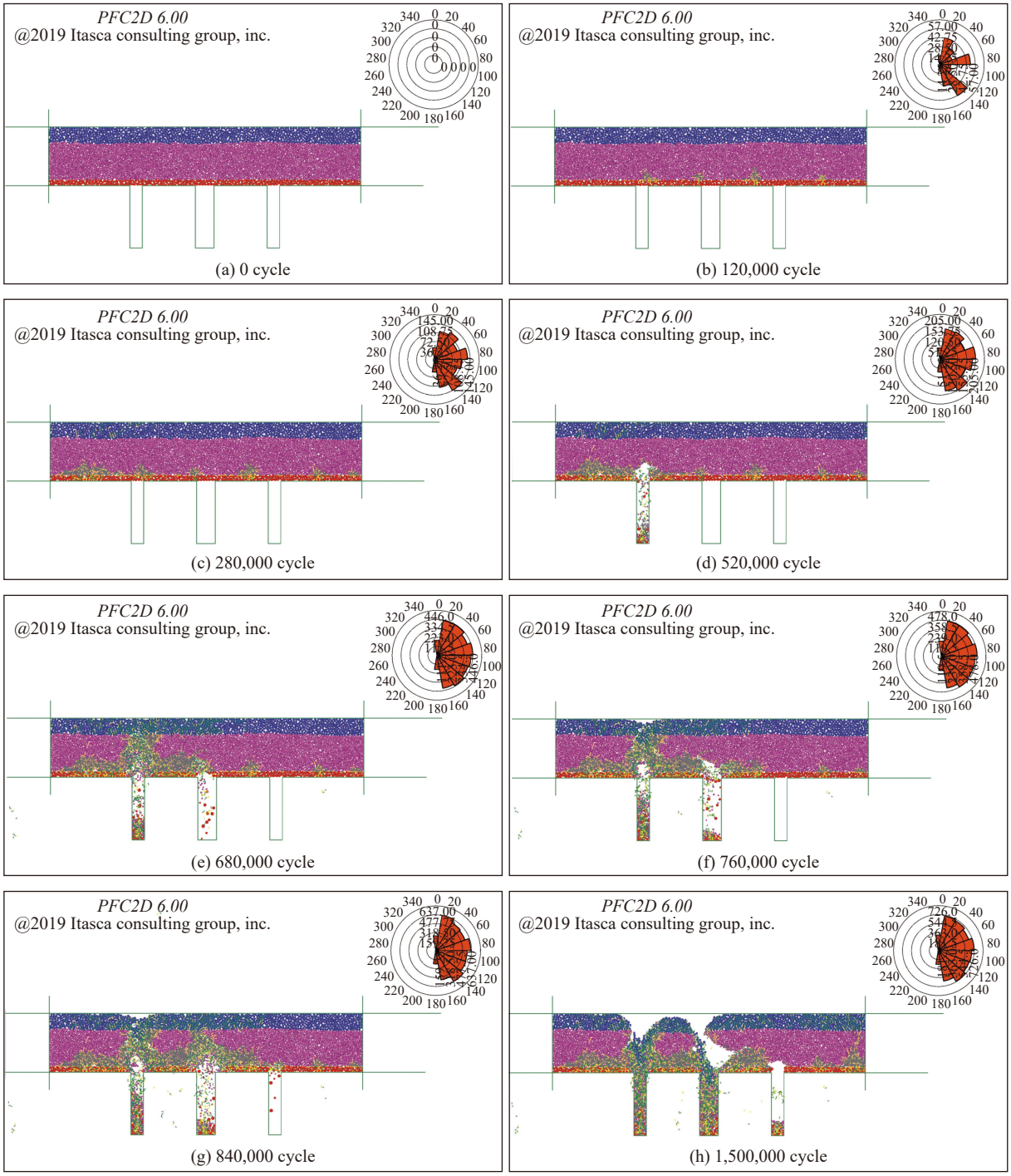


Fig. 14 Collapse evolution process

Critical threshold of collapse caused by negative pressure erosion

The study area features dolomite bedrock beneath laterite and plain fill. Borehole data reveal an average overburden thickness of 9 m, with karst cavities averaging 3 m in diameter. Laboratory tests indicate a laterite uniaxial compressive strength of 150 kPa, with a cohesion coefficient of 1.5. Field investigations provided geomechanical parameters: Unit weight (γ) of 17 kN/m^3, cohesion (c) of 48.3 kPa, and an internal friction angle (φ) of 7.8°. The coefficient of earth pressure at rest (k_0) is 0.5, as per the Geotechnical Engineering Manual. COMSOL simulations assessed safety factors at 60 kPa pressure differential increments. Overburden thickness varies from 3.3 m to 20.9 m. Critical soil-arching thickness, calculated according to Wang (2011), ranges from 2.472 m to 20.072 m. Safety factor variations with respect to average cavity diameter were analyzed across this range at 3 m

decrements (Fig. 15). Results show instability at critical arching thicknesses ≤2 m when pressure differentials reach 100 kPa. However, the likelihood of this scenario is low due to restricted soil cavity-to-arch transition. Overall stability is maintained across all thicknesses for average cavity diameters.

Statistical analysis of karst cave heights, as revealed by boreholes in the study area, indicates a development range of 0 m to 15 m. To thoroughly assess the area's conditions, an extreme assumption was made that the cave's height equals its diameter. This assumption facilitates the evaluation of safety factors across varying cave diameters and overburden thicknesses. Notably, caves with heights under 5 m comprise over 90% of those in the area, predominantly near the rock-soil interface. Thus, the cave diameter was analyzed in increments from 1 m to 5 m. Results are depicted in Fig. 16.

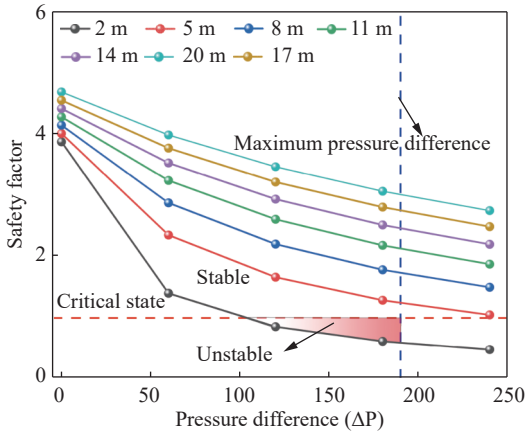


Fig. 15 Variation curve of soil arching thickness with factor of safety (D' = 3 m)

The figures illustrate that for cave diameters of [0,1] m (Fig. 16a), the overburden stability in the study area remains largely unaffected, indicating a stable state. For diameters of [1,2] m (Fig. 16b), the critical overburden thickness is 2 m, with the stability factor dropping below 1 when the pressure differential reaches (150, 190] kPa. As the diameter increases to [3,4] m (Fig. 16c), a critical overburden thickness of 2–5 m results in a safety factor less than 1 under pressure differentials of (60, 190] kPa. At [4,5] m (Fig. 16d), the same critical thickness (2–5 m) yields a safety factor below 1 for pressure differentials of (50, 190] kPa. For diameters of [5,6] m (Fig. 16e), a critical thickness of 2–8 m corresponds to safety factors below 1

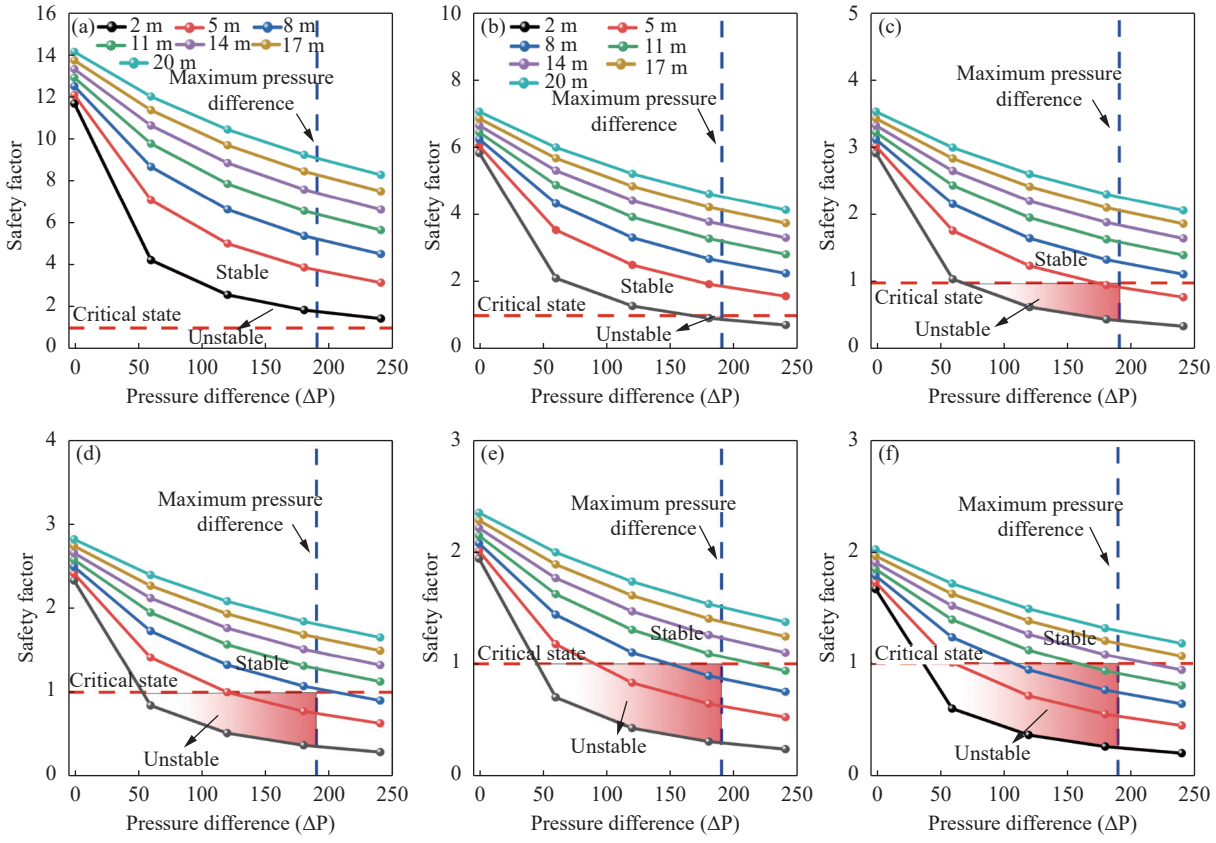


Fig. 16 Variation curves of soil arching thickness with factor of safety (a) D' = 1 m, (b) D' = 2 m, (c) D' = 4 m, (d) D' = 5 m, (e) D' = 6 m, and (f) D' = 7 m

under pressure differentials of (40, 190] kPa. Similarly, atdiameters of [6,7] m (Fig. 16f), the critical thickness of 2–8 m results in safety factors below 1 for pressure differentials of (30, 190] kPa. Overall, the critical overburden thickness range of 2–5 m is identified as a high-risk zone for negative-pressure erosion under typical water-level fluctuations in the study area.

3.3 Collapse risk assessment

Utilizing borehole data from the site, a karst collapse susceptibility assessment indicator system was developed. Employing a comprehensive evaluation model integrated with GIS's spatial analysis module, the karst collapse susceptibility index was computed based on the weighted significance of each indicator. The mathematical model for this susceptibility assessment is as follows:

$$K = W_{B1} \cdot B1 + W_{B2} \cdot B2 + \cdots\cdots + W_{B8} \cdot B8 = \sum_{i=1}^{8} W_{Bi} \cdot Bi \quad (5)$$

Where: K is the discriminant index for collapse susceptibility, representing the assigned value for each influencing factor in the current stratum and denoting the weight of these factors. By conducting pairwise comparisons of the relative importance of each assessment factor, judgment matrices for both the criterion and factor layers were derived as follows:

$$K \sim A = \begin{bmatrix} 1 & 1/2 & 2 \\ 2 & 1 & 3 \\ 1/2 & 1/3 & 1 \end{bmatrix} \quad (6)$$

$$A1 \sim B = \begin{bmatrix} 1 & 2 & 3 \\ 1/2 & 1 & 1/3 \\ 1/3 & 3 & 1 \end{bmatrix} \quad (7)$$

$$A2 \sim B = \begin{bmatrix} 1 & 1/3 & 1/5 \\ 3 & 1 & 1/3 \\ 5 & 3 & 1 \end{bmatrix} \quad (8)$$

$$A3 \sim B = \begin{bmatrix} 1 & 2 \\ 1/2 & 1 \end{bmatrix} \quad (9)$$

By integrating the judgment matrices of the criterion and factor layers, we determined the final weights of each evaluation factor relative to the target layer. This was achieved by aggregating the weights from the factor layer to the criterion layer and from the criterion layer to the target layer. With a Consistency Ratio (CR) of approximately 0.0078, the matrices demonstrate acceptable consistency. The results are detailed in Table 4.

The Analytic Hierarchy Process (AHP) was employed to determine the weights of each indicator and classify their influence levels on karst collapse susceptibility. Normalized indices were assigned accordingly. Using GIS spatial analysis tools, the weighted overlay of index values for all evaluation factors was performed. The graded indicator maps are presented in Fig. 17. To further evaluate karst collapse risk in the study area, the eight evaluation indicators were classified and scored as shown in Table 5.

Using the established karst collapse susceptibility model, we evaluated the risk in the HxS-PL area of Guiyang ity through the Analytic Hierarchy Process (AHP). Theoretical calculations in Chapter 2 reveal that the primary risk is negative-pressure erosion, influenced mainly by cave diameter and overburden thickness. The highest risk is observed when the overburden is 2–8 m thick, particularly when cave diameters exceed 3 m, indicating a significant collapse potential. Based on these thresholds, the area is divided into medium-to-high and low-risk zones, as shown in Fig. 18. The figure indicates that most of the area lacks the conditions necessary for collapse, with high-risk zones confined to the southern sector, covering about 253.15 m^2 (2.3% of the total area). Verification analysis shows that these high-risk areas are primarily due to spatial interpolation suggesting thin overburden and large cave heights, necessitating field validation to confirm actual collapse risk. Overall, the structural stability of the area is largely intact, with a low risk of collapse.

4 Conclusions

(1) Geophysical prospecting, drilling, and field investigations have delineated the overburden, bedrock, and karst cave development in the study area. Vertically developed karst cave and fissure zones have been identified, establishing the lower boundary of karst development at 70 m.

(2) A multi-scale characterization index system for karst media has been developed. At the macro

Table 4 Weights of influence of evaluation factors on karst collapse susceptibility

	B1	B2	B3	B4	B5	B6	B7	B8
Weights	0.1565	0.0757	0.0647	0.0598	0.1682	0.311	0.094	0.0546

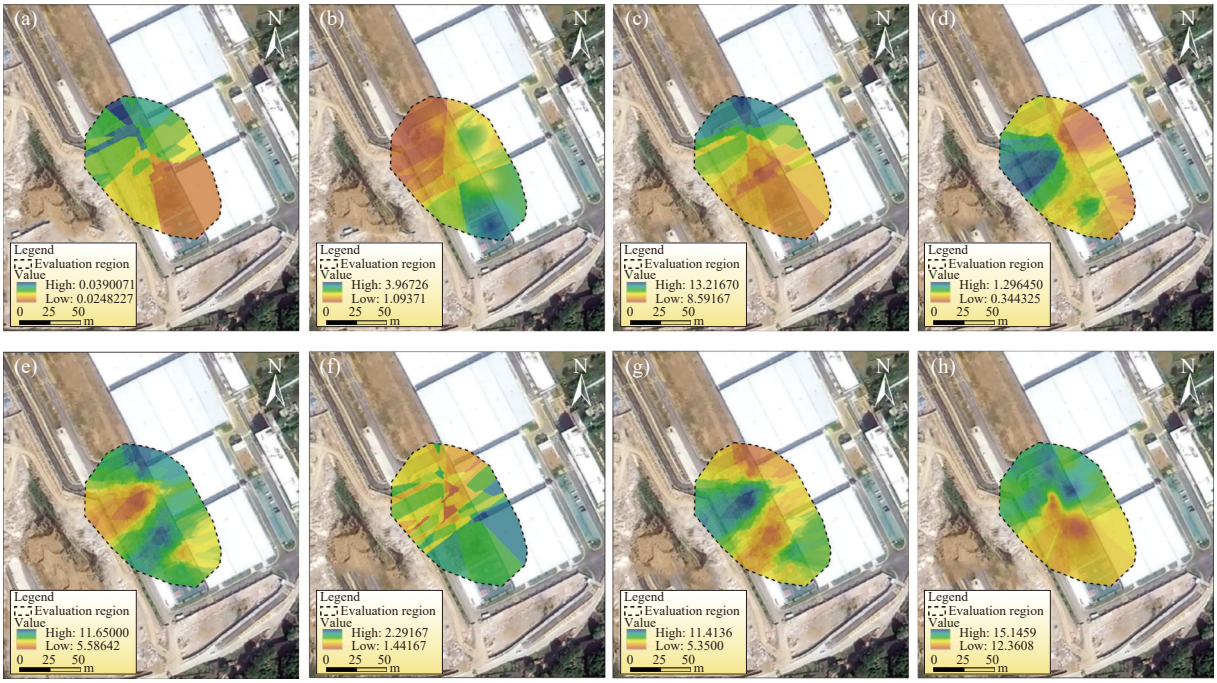


Fig. 17 Spatial interpolation results of evaluation indicators: (a) borehole encounter rate of caves, (b) cave development height (m), (c) cave development depth (m), (d) overburden structure, (e) overburden thickness (m), (f) distance from overburden to cave roof (m), (g) groundwater level depth below overburden (m), (h) depth to phreatic water level (m)

Table 5 Classification and scoring criteria for evaluation factors

Evaluation indicators		**Classification and scoring**		
Criterion layer	Factor layer	1	2	3
Karst development intensity (A1)	Borehole karst encounter rate (B1)	<0.029	0.029–0.034	>0.034
	Karst cave development height (B2)	<1.85	1.85–2.77	>2.77
	Karst cave development depth (B3)	>11.4	10–11.4	<10
Overburden characteristics (A2)	Overburden structure (B4)	>0.97	0.66–0.97	<0.66
	Overburden thickness (B5)	>9.5	7.9–9.5	<7.9
	Distance to karst cave roof (B6)	>2	1.72–2	<1.72
Hydrodynamic conditions (A3)	Groundwater level distance to overburden base (B7)	>9.4	7.3–9.4	<7.3
	Groundwater level to phreatic surface distance (B8)	>14.2	13.2–14.2	<13.2

scale (10^{-1}–1 m), Rock Quality Designation (RQD) and karst rate are employed to define karst development zones. At the meso scale (10^{-3}–10^{-1} m), the fractal dimension of solution holes is utilized to assess the heterogeneity and dissolution intensity of the karst medium. At a finer micro scale (10^{-6}–10^{-3} m), the length of the throat channel and tortuosity are used to differentiate between solution pore and fracture medium types.

(3) The fluctuation amplitude of karst cave water reaches 10 m, with the water level lagging approximately five days behind rainfall. Extreme rainfall can cause a 1.5 m rise in a single day, while the maximum fluctuation over five days is 3.5 m. The general pattern shows rapid alternating rises and falls in the groundwater level during the wet season, with minimal net changes in water level. Conversely, during the dry season, the water level steadily declines, exhibiting significant changes.

(4) Simulation results of actual water level monitoring indicate that, under normal conditions, the continuous variation in rock and soil interface pressure ranges from −62.2 kPa to −190 kPa. This is primarily due to a negative pressure suction effect, although localized failure events also occur. The critical overburden thickness, identified as the high-risk zone for negative pressure suction, is between 2 m and 5 m.

(5) The stability of the study area was assessed

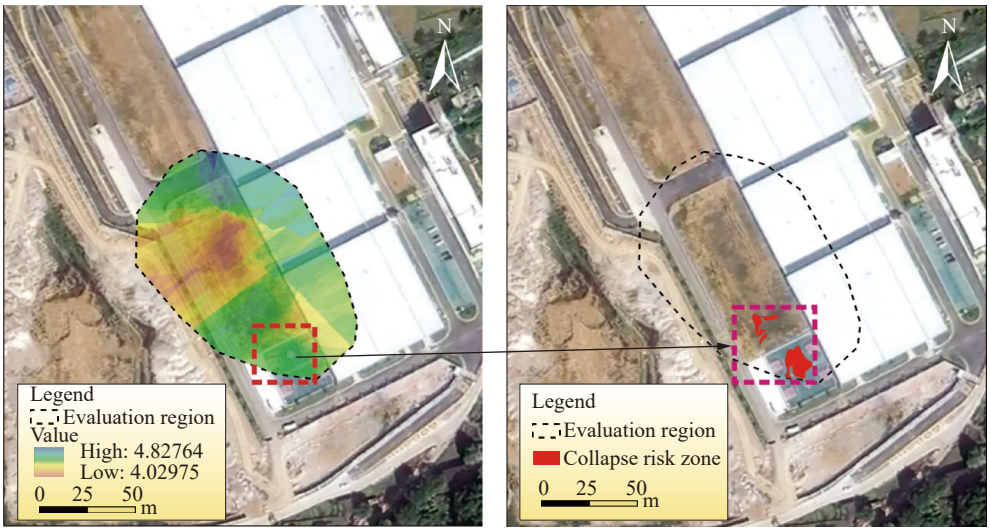


Fig. 18 Comprehensive evaluation results of karst collapse susceptibility in the study area

using multi-field coupling simulation and the Analytic Hierarchy Process (AHP). Findings indicate that under normal water level fluctuations, the area remains stable with no risk of karst collapse. However, extreme conditions, such as engineering disturbances and groundwater exploitation, can lead to rapid depletion of karst cave water, increasing the risk of ground collapse. Most of the study area lacks the fundamental conditions for collapse, with the risk primarily concentrated in the southern region, encompassing approximately 253.15 m^2, representing 2.3% of the total area.

Acknowledgements

This work was funded by the National Key Research and Development Program (Grant Number: 2022YFC300330) and the Fundamental Research Funds for the Central Public Research Institutes (Grant Number: SK202422; SK202310).

References

Ba X, Li L, Wang J, et al. 2020. Near-surface site investigation and imaging of karst cave using comprehensive geophysical and laser scanning: A case study in Shandong, China. Environmental Earth Sciences, 79: 298. DOI：10.1007/s12665-020-09042-y.

Cui QL, Shen SL, Xu YS, et al. 2015. Mitigation of geohazards during deep excavations in karst regions with caverns: A case study. Engineering Geology, 195: 16−27. DOI：10.1016/j.enggeo.2015.05.024.

Cui QL, Wu HN, Shen SL, et al. 2015. Chinese karst geology and measures to prevent geohazards during shield tunnelling in karst region with caves. Nat Hazards, 77: 129−152. DOI：10.1007/s11069-014-1585-6.

Feng Y. 2020. Study on collapse mechanism and prevention measures of dissolution trough zone in Guiyang Metro Line 2. M. S. thesis. Chengdu: Southwest Jiaotong University, 44−46. (in Chinese) DOI：10.27414/d.cnki.gxnju.2020.001688.

He K, Jia Y, Chen W, et al. 2014. Evaluation of karst collapse risks induced by over-pumping and karst groundwater resource protection in Zaozhuang region, China. Environmental Earth Sciences, 71: 3443−3454. DOI：10.1007/s12665-013-2425-9.

He K, Jia Y, Wang B, et al. 2013. Comprehensive fuzzy evaluation model and evaluation of the karst collapse susceptibility in Zaozhuang Region, China. Natural Hazards, 68: 613−629. DOI：10.1007/s11069-013-0642-x.

Kang YS, Geng Z, Lu LH, et al. 2021. Compound karst cave treatment and waterproofing strategy for EPB shield tunnelling in karst areas: A case study. Frontiers in Earth Science, 9: 761573. DOI：10.3389/feart.2021.761573.

Ling CP, Zhang Q. 2024. Exploring the groundwater response to rainfall in a translational landslide using the master recession curve method and cross-correlation function. Journal of Groundwater Science and Engineering, 12(3): 237−252. DOI：10.26599/JGSE.2024.9280018.

Li LP, Sun SQ, Wang J, et al. 2020. Experimental study of the precursor information of the water inrush in shield tunnels due to the proximity of a water-filled cave. International Journal of Rock Mechanics and Mining Sciences, 130: 104320. DOI：10.1016/j.ijrmms.2020.104320.

Liu N, Pei JH, Cao CY, et al. 2022. Geological investigation and treatment measures against water inrush hazard in karst tunnels: A case study in Guiyang, Southwest China. Tunnelling and Underground Space Technology, 124: 104491. DOI：10.1016/j.tust.2022.104491.

Shen SL, Wu HN, Cui YJ, et al. 2014. Long-term settlement behaviour of metro tunnels in the soft deposits of Shanghai. Tunnelling and Underground Space Technology, 40: 309−323. DOI：10.1016/j.tust.2013.10.013.

Wang B, Li ZG, Dong X, et al. 2011. Study on mechanical model of karst collapse: A case of Dongyanglou karst collapse in Tai'an City. Journal of Natural Disasters, 20: 119−125. (in Chinese) DOI：10.13577/j.jnd.2011.0419.

Wang GF, Lyu HM, Jack SS, et al. 2017. Evaluation of environmental risk due to metro system construction in Jinan, China. International Journal of Environmental Research and Public Health, 14(10): 1114. DOI：10.3390/ijerph14101114.

Wang J, Liu L, Zhang Y, et al. 2018. Karst detection and engineering verification of foundation pit in Guiyang metro station by multichannel transient Rayleigh wave method. Progress in Geophysics, 33: 2588−2596. (in Chinese) DOI：10.6038/pg2018BB0177.

Yang ZP, Gao YH, He KJ, et al. 2025. Risk prediction of karst collapse based on susceptibility and rainfall threshold. Chinese Journal of Underground Space and Engineering, 21: 672−683. (in Chinese) DOI：10.20174/j.JUSE.2025.02.35.

Yao WY, Shen SL. 2018. Comprehensive critical mechanical model of covered karst collapse under the effects of positive and negative pressure. Bulletin of Engineering Geology and the Environment, 77: 177−190. DOI：10.1007/s10064-016-0972-5.

Yang L, Cheng YP, Wen XR, et al. 2024. Development, hotspots and trend directions of groundwater numerical simulation: A bibliometric and visualization analysis. Journal of Groundwater Science and Engineering, 12(4): 411−427. DOI：10.26599/JGSE.2024.9280031.

Zhang K, Zheng WB, Liao ZY, et al. 2022. Risk assessment of ground collapse along tunnels in karst terrain by using an improved extension evaluation method. Tunnelling and Underground Space Technology, 129: 104669. DOI：10.1016/j.tust.2022.104669.

Zhang KN, Zhang Y, Liao Y, et al. 2018. Analysis of karst development characteristics and water inrush mode of a metro station in Guiyang. Carsologica sinica, 37: 300−306. (in Chinese) DOI：10.11932/karst20180218.

Zhang L, Xiang XQ, Cheng HH, et al. 2025. Time series InSAR deformation characteristic analysis and early identification of clustered karst collapse groups. Science Technology and Engineering, 25: 4857−4863. (in Chinese) DOI：10.12404/j.issn.1671-1815.2403924.

Zhang LG, Zhu XH, Tuo HT, et al. 2022. Research and application of novel spherical tungsten carbide cutter in shield tunneling engineering of Guiyang karst stratum. Modern Tunnelling Technology, 59: 252−257. (in Chinese) DOI：10.13807/j.cnki.mtt.2022.02.029.

Zhou ZL, Zhang K, Zhang H, et al. 2022. Risk assessment of surface collapse in karst tunnel based on attribute recognition theory. China Safety Science Journal, 32: 105−112. (in Chinese) DOI：10.16265/j.cnki.issn1003-3033.2022.11.1867.